

Construction and evolution of knotted vortex tubes in incompressible Schrödinger flow

Cite as: Phys. Fluids **33**, 077112 (2021); <https://doi.org/10.1063/5.0058109>

Submitted: 27 May 2021 • Accepted: 23 June 2021 • Published Online: 15 July 2021

 Rui Tao (陶瑞),  Hongxiang Ren (任鸿翔),  Yunjin Tong (童云晋), et al.

COLLECTIONS

 This paper was selected as an Editor's Pick



[View Online](#)



[Export Citation](#)



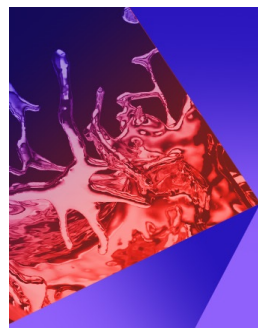
[CrossMark](#)

ARTICLES YOU MAY BE INTERESTED IN

Construction of knotted vortex tubes with the writhe-dependent helicity
Physics of Fluids **31**, 047101 (2019); <https://doi.org/10.1063/1.5088015>

Unsteady flow structures behind a shark denticle replica on the wall: Time-resolved particle image velocimetry measurements
Physics of Fluids **33**, 075109 (2021); <https://doi.org/10.1063/5.0057699>

Turbulent energy cascade associated with viscous reconnection of two vortex rings
Physics of Fluids **33**, 085117 (2021); <https://doi.org/10.1063/5.0058317>



Physics of Fluids

Special Topic: Paint and Coating Physics

Submit Today!

Construction and evolution of knotted vortex tubes in incompressible Schrödinger flow

EP

Cite as: Phys. Fluids 33, 077112 (2021); doi: 10.1063/5.0058109

Submitted: 27 May 2021 · Accepted: 23 June 2021 ·

Published Online: 15 July 2021



View Online



Export Citation



CrossMark

Rui Tao (陶瑞)¹, Hongxiang Ren (任鸿翔)¹, Yunjin Tong (童云晋)², and Shiying Xiong (熊诗颖)^{2,a)}

AFFILIATIONS

¹College of Navigation, Dalian Maritime University, Dalian 116026, China²Department of Computer Science, Dartmouth College, Hanover, New Hampshire 03755, USA^{a)}Author to whom correspondence should be addressed: shiying.xiong@dartmouth.edu

ABSTRACT

We propose a theoretical method for constructing an initial two-component wave function that can be transformed into a knotted velocity field with finite kinetic energy and enstrophy. The wave function is constructed using two complex-valued polynomials, with one determining the desired shape of the knotted central axis and the other encoding the twisting nature of vortex lines, which facilitates the study of helicity conversions. We construct six knotted vortex fields with various centerline and twist helicity as initial conditions for direct numerical simulation of incompressible Schrödinger flow (ISF) in a periodic box. Although the evolution of morphological structure is similar for ISF and classical viscous flow, with all the knots becoming untied after a short time to form one or more separate vortex rings, their statistics are quite different. During the critical period of vortex reconnection, the increase in enstrophy is much more moderate in ISF than in viscous flow, indicating that the Landau–Lifshitz term in ISF inhibits the energy cascade from large to small scales. We also find that the centerline helicity changes dramatically during reconnection, which is consistent with the evolution of the geometrical shape of vortex lines.

Published under an exclusive license by AIP Publishing. <https://doi.org/10.1063/5.0058109>

I. INTRODUCTION

In fluid mechanics, helicity, as an invariant in ideal flows,¹ possesses certain conservation properties in viscous flows,^{2–4} as well as playing a significant role in a wide range of applications. In particular, helicity can measure the topological and geometrical relationships of the links and knots in various physical systems, such as viscous fluids,^{5–9} magnetohydrodynamics flows,^{10–12} liquid crystals,¹³ optical,¹⁴ and biological structures,^{15–17} and cosmic strings.^{18,19} This property provides promising insights into the principles of the breaking and reconnection of flow structures and the mechanism of energy release.^{20,21}

For the flow field of a vortex tube, helicity can be decomposed into two components, namely, the centerline helicity generated by the vortex axis and the twist helicity generated by the vortex line around the axis.²² For an isolated vortex tube in viscous flow, the dynamics is mainly determined by the centerline helicity.^{20,23} However, in the presence of nonconservative forces, such as electromagnetic²¹ and elastic forces,²⁴ the twist helicity cannot be ignored. In addition, the interaction between vortex tubes can lead to conversion between centerline and twist helicity.

Although tracking conversions of conserved quantities between the two components of helicity can provide insight into certain fluid phenomena,² these conversions are challenging to study from a

numerical perspective.²⁵ The total helicity is a simple volume integral of the inner product of the velocity field and the vorticity field; however, separate calculation of the two components faces problems owing to the difficulty of extracting the centerline helicity from the velocity–vorticity field and the twist helicity associated with each vortex line within the entire flow field.¹⁰ Therefore, it is not easy to characterize the conversion between centerline and twist helicity based on the velocity–vorticity field in a continuum dynamics approach.

By contrast, numerical algorithms are available for extracting the tubular structure of wave function (complex function) fields²⁶ to calculate each component of the helicity. Wave functions are generally used to describe quantum mechanical phenomena and, therefore, to employ them for investigating the relationship between centerline helicity and twist helicity; it is necessary to find a way of converting the “continuum mechanics” described by the velocity–vorticity field to the “quantum mechanics” described by the wave function. In this context, the relationship between the velocity–vorticity field and the wave function can be considered to be analogous to that between macroscopic mechanics and quantum mechanics, and this is a topic upon which researchers have been working for many years.

There have been a few attempts to study the conversion between the dynamical equations of fluid mechanics and Schrödinger’s

equation of quantum mechanics under certain conditions. Madelung constructed a correspondence between the velocity field and a single-component wave function and also proved the equivalence between a single-component linear Schrödinger equation and the compressible Euler equations.^{27,28} Hasimoto converted a local induced approximation of vortex filaments into nonlinear Schrödinger equations, as well as proving that solitary waves can propagate on a vortex filament by finding solitary wave solutions of a nonlinear Schrödinger equation.^{29–31} These transformations provide us with a new perspective to understand the relationship between continuum mechanics and quantum mechanics. However, in the process of transformation, the fluid system is significantly simplified. For example, in the Madelung transformation, the fluid flow is described in terms of the gradient of the phase angle of the wave function, which means that it is a potential flow without vorticity. In Hasimoto's approach, the fluid is assumed to contain isolated vortex filaments that exhibit discontinuities throughout the computational field, and consequently, it is not possible to demonstrate complete continuous evolution of the fluid flow in the quantum mechanical system.

To represent a velocity field with nonzero vorticity, it is necessary to increase the number of wave function components. Schoenberg established a correspondence between the velocity field and a multi-component wave function.³² Furthermore, Sorokin extended the Madelung transformation to a two-component wave function, making it possible to describe a flow with nontrivial vorticity or even nontrivial helicity using a two-component Schrödinger equation.³³ Most recently, Chern *et al.*³⁴ simulated flow evolution using a two-component Schrödinger equation and demonstrated a considerable number of classic fluid mechanical phenomena. The flow field described by the two-component wave function, called incompressible Schrödinger flow (ISF), serves as the basis for our work here.

Compared with the dynamical evolution governed by the classical Navier–Stokes equations, the simulation of ISF exhibits better structure conservation and flow stability. The structure conservation of ISF is guaranteed by the fact that the intrinsic dynamics is represented by a Hamiltonian system,³⁵ whose energy function is the kinetic energy of the ideal fluid together with an energy of the Landau–Lifshitz type.³⁶ Moreover, the Landau–Lifshitz energy enhances the stability of flow evolution and the retention of tube-shaped vortex structures. Therefore, to simulate ISF, we can adopt a computational scale smaller than that for viscous flow governed by the Navier–Stokes equations while maintaining the classic vortex structure in the simulation process. However, owing to the necessity of constructing initial conditions using an intricate numerical method to simulate the evolution of ISF,³⁷ it is difficult to perform thorough quantitative investigations on the physical parameters and quantities during ISF evolution.

This paper proposes a theoretical method for constructing an initial two-component wave function that can be transformed into a knotted velocity field with arbitrary complexity. Inspired by the rational map,³⁸ we use two complex-valued polynomials of the complex coordinates on the unit three-sphere to construct the wave function. Specifically, the first polynomial is used to design the desired shape of the knotted central axis, and the second is chosen to encode the twisting nature of vortex lines. Thus, this method can be used to construct a vortex tube with arbitrary geometry and topology specified by the two given complex-valued polynomials, and it appears to be more flexible for constructing complex vortex knots than those methods that

rely on an optimized Seifert surface.^{34,39,40} Since both polynomials used to construct the wave function are tunable, this vortex construction can facilitate investigation of the conversion between centerline helicity and twist helicity.^{41–43} Furthermore, the constructed fields with finite kinetic energy and enstrophy can be used as the initial states of numerical simulations.

As examples, we construct six initial knotted vortex tubes with different centerline and twist helicity. These knotted fields are used as initial conditions in the direct numerical simulation (DNS) of ISF in a periodic box. Specifically, we simulate ISF using a pseudospectral method⁴⁴ and quantitatively analyze the dynamical information during the evolution of knotted vortex tubes. Similar to the evolution in viscous flow,^{20,21} the knotted vortex tubes in ISF involve significant aspects of vortex dynamics, such as vortex knot untying,⁴⁵ reconnection,^{46–50} and breakdown.⁵¹ Based on the numerical results, we discuss the relationship, similarities, and differences between ISF and viscous flow.^{21,52}

The outline of this paper is as follows. In Sec. II, we introduce the mathematical definitions of Clebsch maps and spherical Clebsch maps. In Sec. III, we propose a theoretical method to construct the initial spherical Clebsch maps for velocity fields with knotted structures and computable helicity components and verify its feasibility with several numerical examples. In Sec. IV, we introduce the governing equations of ISF and the transformation relationship between wave function and velocity field. In Sec. V, we visualize and characterize the numerical results. Some conclusions are drawn in Sec. VI.

II. CLEBSCH MAPS AND SPHERICAL CLEBSCH MAPS

A. Clebsch maps

Established as a Lagrangian description of fluid dynamics in an Eulerian reference frame, a Hamiltonian formulation was first introduced by Clebsch as the Clebsch representation.^{53,54} In the original Clebsch representation,⁵³ the velocity Clebsch potentials (λ, ϕ, μ) are used to represent the velocity in three-dimensional Euclidean space \mathbb{R}^3 as

$$\mathbf{u} = \lambda \nabla \mu - \nabla \phi \quad (1)$$

and the vorticity Clebsch potentials (λ, μ) are then used to represent the vorticity $\boldsymbol{\omega} = \nabla \times \mathbf{u}$ as

$$\boldsymbol{\omega} = \nabla \lambda \times \nabla \mu. \quad (2)$$

From Eq. (2), we can see that the isosurfaces of λ and μ are vortex surfaces,^{55–57} that is, they satisfy $\boldsymbol{\omega} \cdot \nabla \lambda = 0$ and $\boldsymbol{\omega} \cdot \nabla \mu = 0$, respectively. Thus, Clebsch maps contain important geometric information about the flow fields, which provides an appealing perspective for fluid visualization,^{35,58} analysis,⁵⁹ and simulation.^{60,61} However, the original Clebsch maps Eqs. (1) and (2) cannot describe a flow field with non-zero helicity, which imposes limits on their application to natural three-dimensional flows.

B. Spherical Clebsch maps

Based on the pioneering work by Kuznetsov and Mikhailov,⁶² Chern *et al.*^{34,37} proposed spherical Clebsch maps, which overcome the disadvantage of the original Clebsch maps, namely, their inability to represent a velocity–vorticity field with nonzero helicity.

Specifically, the spherical Clebsch maps write the velocity in the form of wave functions,

$$\psi = [\psi_1, \psi_2]^T = [a + ib, c + id]^T \quad (3)$$

with a normalization constraint

$$\langle \psi, \psi \rangle_R = 1 \quad (4)$$

and a solenoidal constraint

$$\langle \Delta\psi, i\psi \rangle_R = 0. \quad (5)$$

Here, i represents the imaginary unit, $\langle \psi, \phi \rangle_R = \text{Re}(\bar{\phi}_1\psi_1 + \bar{\phi}_2\psi_2)$, $\text{Re}(f)$ denotes the real part of a complex-valued function f , and a, b, c, d are all real-valued. The vorticity Clebsch potentials, also called the spin vector, are then expressed in the form of a unit vector field $s = (s_1, s_2, s_3)$ and connected with the wave function by the Hopf fibration⁵³

$$\begin{cases} s_1 = a^2 + b^2 - c^2 - d^2, \\ s_2 = 2(bc - ad), \\ s_3 = 2(ac + bd). \end{cases} \quad (6)$$

In spherical Clebsch maps, the velocity u is represented as

$$u = \hbar \langle \nabla\psi, i\psi \rangle_R = \hbar(a\nabla b - b\nabla a + c\nabla d - d\nabla c), \quad (7)$$

where \hbar is a parameter controlling quantization of velocity–vorticity, and the vorticity ω is represented as

$$\omega = \frac{\hbar}{2}(s_1\nabla s_2 \times \nabla s_3 + s_2\nabla s_3 \times \nabla s_1 + s_3\nabla s_1 \times \nabla s_2). \quad (8)$$

We remark that as with original Clebsch maps, the potential functions (6) are exact vortex surface fields owing to

$$\omega \cdot \nabla s_p = 0, \quad p = 1, 2, 3, \quad (9)$$

since the vortex lines integrated from points on isosurfaces of s_p are perfectly tangent to the isosurfaces. Thus, the isosurfaces of s_p can be used as the initial condition for the evolution of vortex surfaces in a Lagrangian-like study of vortex dynamics.^{52,64–69}

In addition, Eq. (6) fulfills gauge invariance, which means that ψ and its gauge transformation $e^{-iq/\hbar}\psi$ correspond to the same spin vector field s , where q is a scalar gauge function. Moreover, the gauge transformation of the wave function $\psi \rightarrow e^{-iq/\hbar}\psi$ corresponds to the gauge transformation of the velocity $u \rightarrow u - \nabla q$, and the incompressibility condition on the velocity, $\nabla \cdot u = 0$, is equivalent to Eq. (5).

Figure 1 summarizes the equations introduced above. It shows the transformations between the corresponding wave functions ψ , spin vector s , velocity u , and vorticity ω of a vortex ring in different spaces.⁷⁰ The upper left figure depicts a complex structure that is the two-component wave function on the unit three-sphere S^3 . Through the Hopf fibration (6), the spin vector s can be obtained on the unit two-sphere S^2 , which is represented by the patch on the upper right sphere. Given the wave function, we can also calculate the velocity (7), which is shown in the bottom left box. The blue tube with the dotted outline shows the vortex tube.⁷¹ The orange lines around the tube represent the integral lines of u . Given the formulation of u , we use the definition $\omega = \nabla \times u$ to obtain the vorticity, shown in the bottom right box. In the vorticity field, the vortex tube is represented by the blue tube with

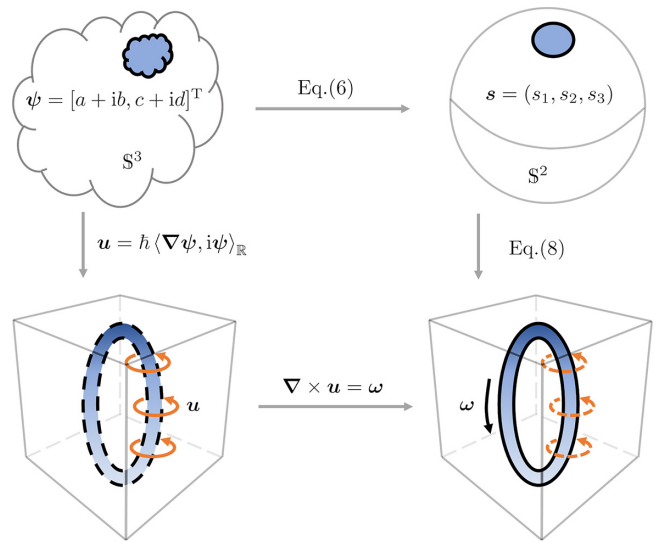


FIG. 1. Relationship between velocity u , vorticity ω , wave function ψ , and spin vector s .

the solid outline, and the dotted orange lines represent the velocity lines. ω can also be defined in terms of the spin vector as Eq. (8).

III. CONSTRUCTION OF SPHERICAL CLEBSCH MAPS

A. Theoretical construction of spherical Clebsch maps

This section proposes a novel method to construct initial spherical Clebsch maps based on the rational maps in Kedia *et al.*³⁸ The method consists of five steps:

1. Transform the Cartesian coordinates $(x, y, z) \in \mathbb{R}^3$ in Euclidean space into the coordinate system $(\alpha, \beta) \in \mathbb{C}^2$ in two-component complex space.
2. Construct a polynomial P to represent the twist of the vortex tube in the coordinate system (α, β) .
3. Construct a scalar function Q in the coordinate system (α, β) to represent the geometric position of the vortex axis.
4. Use Eq. (4) to normalize the wave function.
5. Use Eq. (5) to ensure a divergence-free projection.

The details of this construction are as follows.

1. Transformation of the coordinate system

First, we map the coordinate system from the Euclidean space \mathbb{R}^3 to the two-component complex space \mathbb{C}^2

$$\begin{cases} \alpha = \frac{2(X + iY)f(R)}{1 + R^2}, \\ \beta = \frac{2(Z - i)f(R) + (1 + R^2)i}{1 + R^2}, \end{cases} \quad (10)$$

where $X = \lambda_x(x - x_c)$, $Y = \lambda_y(y - y_c)$, $Z = \lambda_z(z - z_c)$ are scaled and centralized coordinates with scaling numbers $(\lambda_x, \lambda_y, \lambda_z)$ and center coordinates (x_c, y_c, z_c) , $R = \sqrt{X^2 + Y^2 + Z^2}$ is the scaled distance from (x_c, y_c, z_c) , and the function $f(R)$ decays monotonically with

$f(0) = 1$ and $\lim_{R \rightarrow \infty} f(R) = 0$. We remark that Eq. (10) maps a Euclidean space to a compact space, since

$$|\alpha|^2 + |\beta|^2 = 1 + \frac{4f(f-1)}{1+R^2} \leq 1. \quad (11)$$

Thus, Eq. (10) maps a trivial structure in infinite space to a complex knotted structure in finite space.³⁸

2. Complex polynomial function P

P is constructed to represent the twist of the vortex tube, i.e., the degree to which the vortex filament in the tube spirals around the axis. In general, we construct polynomials

$$P = \alpha^k \quad (12)$$

to represent the degree of twist degree of the vortex tube. The larger the value of k , the more twisted is the vortex tube. It is worth noting that since normalization affects the degree of twist, we cannot precisely and quantitatively describe the influence of k on the twist helicity.

3. Complex polynomial function Q

We construct the wave function Q to represent the geometric shape of the vortex structure, with the contour line corresponding to $Q=0$ representing the vortex axis of the vortex tube. Weißmann *et al.*²⁶ have provided a numerical method to construct Q for a given velocity field, in which ψ is determined by solving the optimization problem

$$\begin{cases} Q = \underset{\psi}{\operatorname{argmin}} |\hbar \nabla \psi - i \mathbf{u} \psi|, \\ \text{s.t. } \int_{\Omega} |\psi| d\Omega = 1, \end{cases} \quad (13)$$

where Ω denotes the entire flow domain. We remark that the convexity of such optimization problems has not been proved, and it is unknown whether the numerical solution for the wave function is smooth over the whole field. Thus, there are still some theoretical and technical problems that need to be addressed to solve Eq. (13) directly. In this paper, we focus on the construction of Q based on an analytic expression, in which we construct the analytic expression for the wave function Q to represent the knotted vortex filaments of a series of complex geometrical topologies. The polynomial function

$$Q = Q(\alpha, \beta, \bar{\alpha}, \bar{\beta}), \quad (14)$$

in which α and β are given by Eq. (10), can express a series of knotted link structures. For example, the zero level line of $Q = \alpha^3 + \beta^2$ is a trefoil knot.

4. Normalization

We normalize P and Q as

$$P^* = \frac{P}{\sqrt{|P|^2 + |Q|^2}}, \quad Q^* = \frac{Q}{\sqrt{|P|^2 + |Q|^2}}. \quad (15)$$

5. Pressure projection

Finally, we take the divergence-free projection of Eq. (15) as

$$\psi_1 = P^* e^{-iq/\hbar}, \quad \psi_2 = Q^* e^{-iq/\hbar}, \quad (16)$$

where the pressure-like variable q is calculated as

$$\Delta q = \hbar \langle \Delta \psi, i \psi \rangle_{\mathbb{R}}. \quad (17)$$

We remark that we use Eqs. (10), (12), and (14)–(16) to construct the knotted wave function and compute the knotted velocity field through Eq. (7). Note that although we have alternative ways to construct knotted fields numerically or analytically, we cannot analytically solve for the wave function from an arbitrary given velocity field. The reason is that for a general velocity field, there is no known way to solve Eq. (7) analytically, and sometimes the solution does not even exist. If we want to get an approximate wave function from a given velocity field, we can obtain a numerical solution for the wave function by minimizing the Dirichlet energy³⁷

$$E^\epsilon(\psi) = \int_{\Omega} \left(\frac{1}{\hbar^2} |\mathbf{u} - \hbar \langle \nabla \psi, i \psi \rangle|^2 + \frac{\epsilon}{4} |\nabla s|^2 \right) d\Omega, \quad (18)$$

where ϵ is a regularization parameter and $d\Omega$ is the volume element. However, each component of the two-component wave function constructed by this method has no physical significance.

B. Numerical cases

We construct six cases to study the evolution of knots with different shapes and twists. Since the polynomials $P(\alpha, \beta, \bar{\alpha}, \bar{\beta})$ and $Q(\alpha, \beta, \bar{\alpha}, \bar{\beta})$ control the twist and shape of the knots, respectively, we set different initial conditions for the numerical simulation, namely, $(P, Q) = (\alpha^m, \alpha^l + \beta^2)$, $m = 1, 3, 5$, $l = 3, 5$, and we set the scaling numbers, the center coordinates, and the decay function in Eq. (10) as $(\lambda_x, \lambda_y, \lambda_z) = (1.2, 1.2, 1.6)$, $(x_c, y_c, z_c) = (\pi, \pi, 0.6\pi)$, and $f(R) = \exp(-R^8/9^4)$, respectively. The parameters $\lambda_x, \lambda_y, \lambda_z$ and x_c, y_c, z_c are chosen to ensure that the size and position of the constructed knots are reasonably distributed in the flow domain Ω . We initialize λ_x, λ_y less than λ_z referring to the settings in other papers.^{20,21}

The important parameters and statistics of the constructed initial fields are summarized in Table I, including the volume-averaged kinetic energy $E_u = \int E(k) dk$ with energy spectrum $E(k)$, the volume-averaged enstrophy $E_\omega = 2 \int k^2 E(k) dk$, vorticity flux Γ along the vortex axis, and the helicity $H = \int_Q h d\Omega$ with helicity density $h = \mathbf{u} \cdot \boldsymbol{\omega}$. It can be seen that the constructed fields have finite kinetic energy and enstrophy, and so they can be used as the initial states of the numerical simulation. In addition, these constructed fields have tunable helicity, and so the effect of different helicity on the dynamic evolution of the fluid can be compared. Moreover, we also show in Table I the values of the different helicity components, which we discuss in detail in Sec. III C.

Figure 2 shows the isosurfaces of s_1 of initial knotted vortex tubes with six different wave functions ψ summarized in Table I. The isosurfaces are color-coded by the helicity density h . Some vortex lines are integrated on the surfaces. We observe that the vortex lines are almost on the isosurface of s_1 , which is guaranteed by Eq. (9). The isosurfaces of s_1 in the first row have the shape of a trefoil knot with $Q = \alpha^3 + \beta^2$, while those in the second row have the shape of a cinquefoil knot with

TABLE I. Summary of parameters and statistics in the numerical construction of six different initial knotted fields.

Cases		T1	T3	T5	C1	C3	C5
Polynomial I	P	α	α^3	α^5	α	α^3	α^5
Polynomial II	Q	$\alpha^3 + \beta^2$	$\alpha^3 + \beta^2$	$\alpha^3 + \beta^2$	$\alpha^5 + \beta^2$	$\alpha^5 + \beta^2$	$\alpha^5 + \beta^2$
Kinetic energy	E_u	0.0015	0.0033	0.0047	0.0017	0.0035	0.0052
Enstrophy	E_ω	0.0154	0.0684	0.203	0.0173	0.0611	0.164
Vorticity flux	Γ	0.625	0.628	0.633	0.627	0.628	0.628
Writhe	W_r	3.49	3.49	3.49	6.78	6.78	6.78
Scaled helicity	$H/(2\pi\hbar)^2$	2	6	10	2	6	10
Scaled centerline helicity	$H_C/(2\pi\hbar)^2$	3.45	3.49	3.54	6.77	6.78	6.79
Scaled twist helicity	$H_T/(2\pi\hbar)^2$	-1.45	2.51	6.46	-4.77	-0.783	3.20

$Q = \alpha^5 + \beta^2$. Meanwhile different columns with different $P = \alpha, \alpha^3$ and α^5 correspond to different intrinsic twist.

Figure 3 plots the isosurfaces of $s_p, p = 1, 2, 3$, with different contour values of the trefoil and cinquefoil knotted vortex tubes (cases T1 and C1 in **Table I**). In **Fig. 3(a)**, the isosurfaces of $s_p, p = 1, 2, 3$, show that different s_p identify approximately the same knotted structures. Some vortex lines integrated on the surfaces also agree with Eq. (9). **Figure 3(b)** plots the isosurfaces of s_1 with different contour values from inside to outside.

C. Helicity of the constructed fields

An important feature of spherical Clebsch maps is that they can characterize a flow field with nonzero helicity. In particular, we can write Eq. (3) in hyperspherical coordinate form as

$$(a, b, c, d) = (\cos \phi_1, \sin \phi_1 \cos \phi_2, \sin \phi_1 \sin \phi_2 \cos \phi_3, \sin \phi_1 \sin \phi_2 \sin \phi_3), \quad (19)$$

and substituting this into Eqs. (6)–(8) yields

$$\left\{ \begin{array}{l} \mathbf{u} = \hbar[\cos \phi_2 \nabla \phi_1 - \cos \phi_1 \sin \phi_1 \sin \phi_2 \nabla \phi_2 + (\sin \phi_1 \sin \phi_2)^2 \nabla \phi_3], \\ \boldsymbol{\omega} = 2\hbar \sin \phi_1 \sin \phi_2 (\sin \phi_1 \cos \phi_2 \nabla \phi_2 \times \nabla \phi_3 - \cos \phi_1 \sin \phi_2 \nabla \phi_3 \times \nabla \phi_1 + \sin \phi_1 \nabla \phi_1 \times \nabla \phi_2). \end{array} \right. \quad (20)$$

Then, using Eq. (20), we obtain $\mathbf{u} \cdot \boldsymbol{\omega} = 2\hbar^2 \sin \phi_1^2 \sin \phi_2 \nabla \phi_1 \cdot (\nabla \phi_2 \times \nabla \phi_3)$. Finally, the helicity can be expressed as

$$H = \int \mathbf{u} \cdot \boldsymbol{\omega} d\Omega = 2\hbar^2 \int \sin \phi_1^2 \sin \phi_2 \nabla \phi_1 \cdot (\nabla \phi_2 \times \nabla \phi_3) d\Omega = (2\pi\hbar)^2 n_\psi, \quad (21)$$

where n_ψ is the mapping degree of the wave function ψ . All the computations are performed in a box with periodic boundary conditions. To make the continuity of the wave function compatible with the boundary conditions, n_ψ must theoretically be an integer. It can be seen from **Table I** that this property is strictly satisfied in the constructed initial knotted vortex tubes.

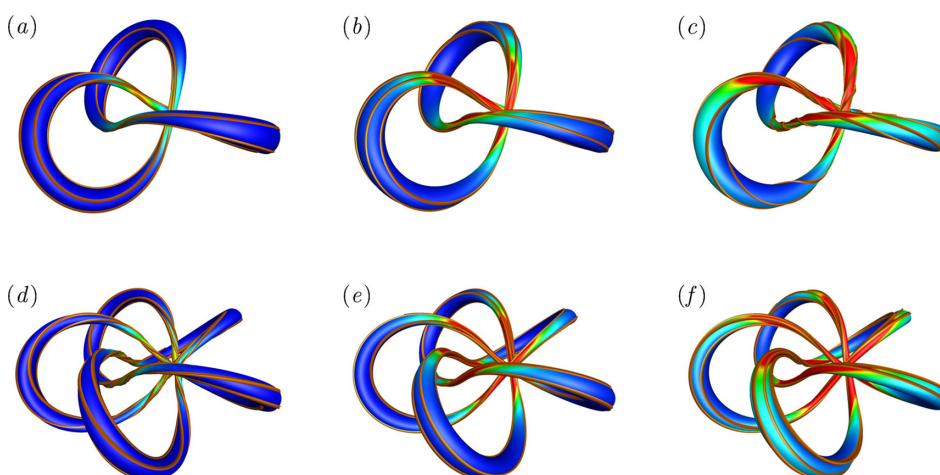


FIG. 2. Isosurfaces of s_1 of initial knotted vortex tubes with six different wave functions ψ . The polynomial functions P and Q for constructing ψ in (16) are summarized in **Table I**. The isosurfaces are color-coded by the helicity density h . Some vortex lines are shown on the surfaces. The corresponding case labels in **Table I** and isocontour values are (a) T1, $s_1 = 0.85$; (b) T3, $s_1 = 0.6$; (c) T5, $s_1 = 0.25$; (d) C1, $s_1 = 0.93$; (e) C3, $s_1 = 0.8$; and (f) C5, $s_1 = 0.56$, respectively.

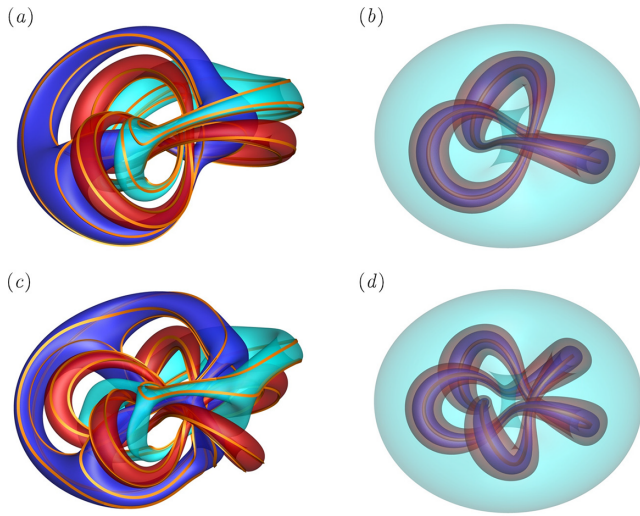


FIG. 3. Isosurfaces of s_p , $p=1, 2, 3$, with different contour values of the trefoil knotted vortex tube (cases T1 and C1 in Table I). (a) and (c) Isosurfaces of $s_1 = 0.8$ (red), $s_2 = 0.9$ (blue), and $s_3 = 0.95$ (cyan). Some vortex lines are integrated on the surfaces. (b) and (d) Isosurfaces of s_1 with contour values of 1, 0.8, 0.5, and -0.8 from inside to outside.

The helicity of a knotted vortex tube consists of two parts. One is the centerline helicity $H_C = \Gamma^2 W_r$, which is completely determined by the central vortex axis, where Γ is the strength of the toroidal vorticity flux along the central axis C and the writhe is defined as

$$W_r = \frac{1}{4\pi} \oint_{C,C} \oint \frac{[\mathbf{T}(s) \times \mathbf{T}(s')] \cdot [\mathbf{c}(s) - \mathbf{c}(s')]}{|\mathbf{c}(s) - \mathbf{c}(s')|^3} ds ds'. \quad (22)$$

Here, s is the arc length parameter, \mathbf{c} is the parametric equation of the central vortex axis, and \mathbf{T} is the unit tangent of the central vortex axis C . The other part is the twist helicity $H_T = \Gamma^2 T_w$, which measures the

degree of twist of vortex lines in the tube around the vortex axis. Also, the twist helicity H_T is the difference between the total helicity and the centerline helicity, $H_T = H - H_C$.

To calculate the helicity component of the flow field, we need to extract the vortex axis of the vortex tube through the wave function. We describe the method for extracting the central vortex axis in [Appendix A](#). In our construction, the vortex axis can be understood as the zero contour of ψ_2 , i.e., $\psi_2 = c + id = 0$.

[Figure 4](#) shows a schematic of the extraction of the vortex axis from the isosurface of ψ_2 of the trefoil and cinquefoil knots at the initial time. We can observe from [Figs. 4\(a\) and 4\(e\)](#) that the isosurface of c has the shape of a knotted tube, while the isosurface of d is a twisted surface whose interior intersects the vortex axis of the knot to form a Seifert surface. The line of intersection of the two scalar fields c and d forms the central vortex axis. The area passed by the vortex axis is usually the place where the height of the isosurface changes sharply. By contrast, the places where the height changes are very small, such as the top of the $c = 0$ isosurface and the outer region of the $d = 0$ isosurface, have no vortex axis.

IV. NUMERICAL SIMULATION

A. Landau–Lifshitz modified fluid

We study the evolution of the knotted vortex tubes constructed using spherical Clebsch maps in a Landau–Lifshitz modified fluid. The governing equations are

$$\begin{cases} \frac{\partial \mathbf{u}}{\partial t} + \mathbf{u} \cdot \nabla \mathbf{u} = -\frac{1}{\rho} \nabla \Pi + \mathbf{f}_{LL}, \\ \nabla \cdot \mathbf{u} = 0, \end{cases} \quad (23)$$

where t is the time and $\rho = 1$ is the constant density,

$$\Pi = \frac{p}{\hbar} - \frac{\hbar}{2} |\nabla \psi|^2 - \frac{\hbar}{4} \langle \mathbf{s}, \Delta \mathbf{s} \rangle + \frac{1}{2} |\mathbf{u}|^2, \quad (24)$$

with pressure p , and the Landau–Lifshitz force is³⁴

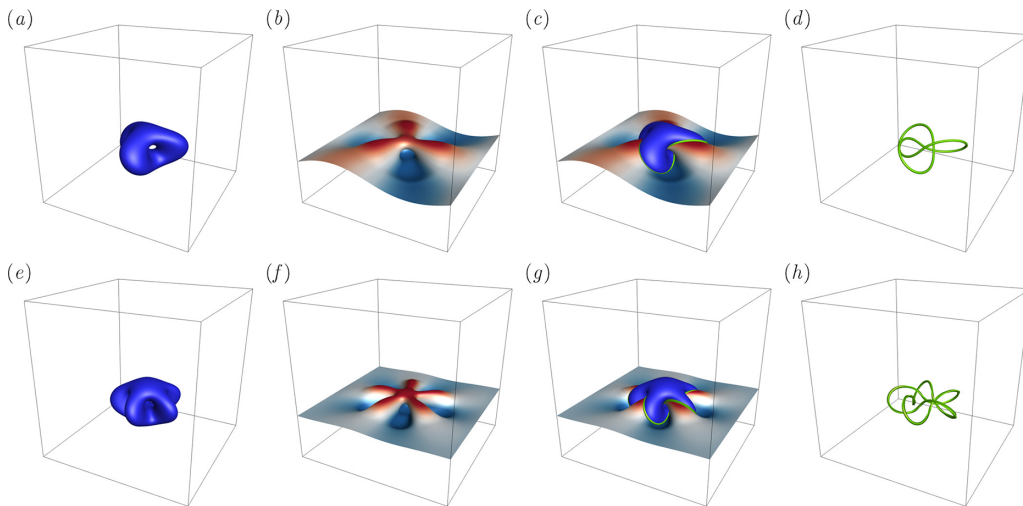


FIG. 4. Extraction of the vortex axis from the isosurface of ψ_2 of the trefoil knot and cinquefoil knot at the initial time, with (a)–(d) corresponding to T1, and (e)–(h) to C1: (a) and (e) $c = 0$ isosurface; (b) and (f) $d = 0$ isosurface; (c) and (g) intersection line of $c = 0$ and $d = 0$ isosurfaces; (d) and (h) vortex axis.

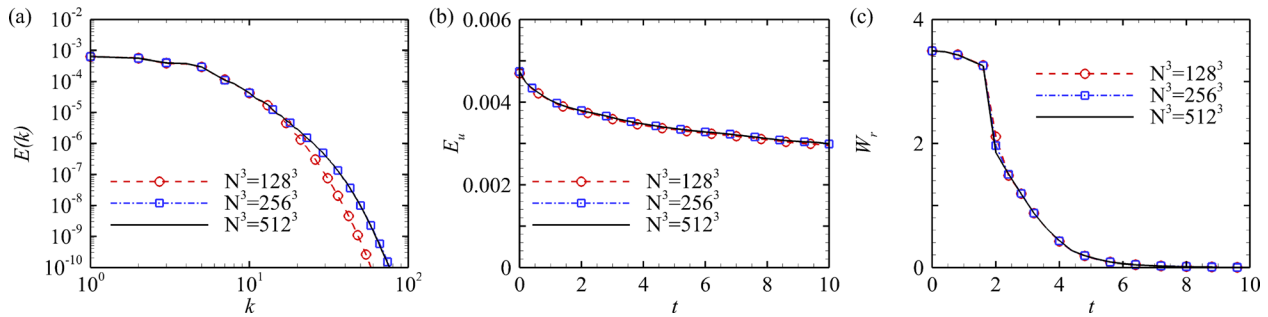


FIG. 5. Statistics of the fluid field with three grid resolutions $N^3 = 128^3, 256^3$ for the case T1 in Table I. (a) Kinetic energy spectrum at $t = 10$. (b) The temporal evolution of the volume-averaged kinetic energy. (c) The temporal evolution of the writhe.

$$\mathbf{f}_{\text{LL}} = -\frac{\hbar^2}{4} (\nabla \mathbf{s}) \cdot \Delta \mathbf{s}. \quad (25)$$

Substituting Eq. (7) into Eqs. (23) and (25) yields the incompressible Schrödinger flow (ISF) (the derivation is in Appendix B),

$$\begin{cases} \frac{\partial \psi}{\partial t} = i \frac{\hbar}{2} \nabla^2 \psi - i \frac{1}{\hbar} P \psi, \\ \langle \Delta \psi, i \psi \rangle_R = 0, \\ |\psi| = 1, \end{cases} \quad (26)$$

with appropriate initial condition $\psi(\mathbf{x}, t = 0) = \psi_0(\mathbf{x})$ and boundary condition (e.g., periodic boundary condition). Thus, we can use the wave functions to simulate ISF in Eq. (26) rather than the velocity field in Eq. (23).^{34,37}

B. Pseudospectral method

DNS of ISF is performed to solve Eq. (26) in a periodic box of side $L = 2\pi$ using a standard pseudospectral method.^{44,72} The computational domain Ω is discretized on uniform grid points N^3 . Aliasing errors are removed using the two-thirds truncation method with maximum wavenumber $k_{\max} \approx N/3$.

Specifically, the Fourier coefficient $\hat{\psi}(\mathbf{k}, t) = \mathcal{F}(\psi)$ with wavenumber \mathbf{k} is advanced in time using an analytic approach as

$$\hat{\psi}^*(\mathbf{k}, t + \Delta t) = \exp\left(-\frac{1}{2}\hbar k^2 \Delta t\right) \hat{\psi}(\mathbf{k}, t), \quad (27)$$

where $k = |\mathbf{k}|$ denotes the wavenumber magnitude and Δt is the time step. The inverse Fourier transform operator \mathcal{F}^{-1} is then used

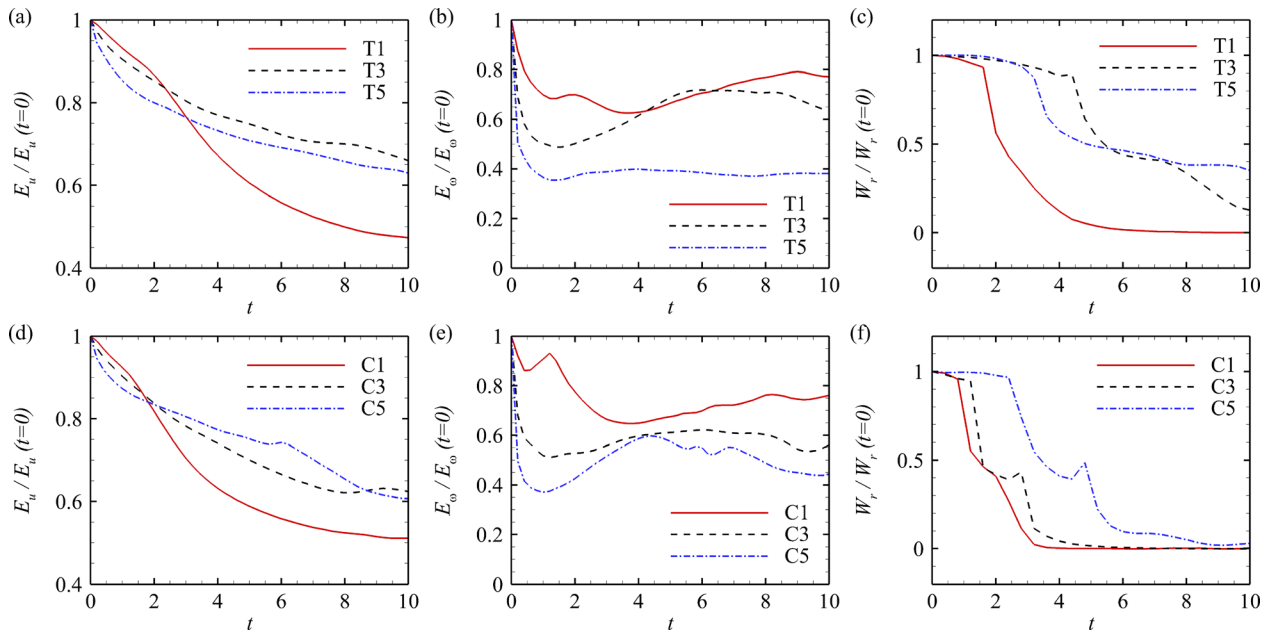


FIG. 6. Temporal evolution of normalized kinetic energy, enstrophy, and writhe: (a) normalized kinetic energy of T1, T3, and T5 from Table I with $Q = \alpha^3 + \beta^2$; (b) normalized enstrophy of T1, T3, and T5 from Table I with $Q = \alpha^3 + \beta^2$; (c) normalized writhe of T1, T3, and T5 from Table I with $Q = \alpha^3 + \beta^2$; (d) normalized kinetic energy of C1, C3, and C5 from Table I with $Q = \alpha^5 + \beta^2$; (e) normalized enstrophy of C1, C3, and C5 from Table I with $Q = \alpha^5 + \beta^2$; (f) normalized writhe of C1, C3, and C5 from Table I with $Q = \alpha^5 + \beta^2$.

to transform $\hat{\psi}^*(\mathbf{k}, t + \Delta t)$ to physical space: $\psi^*(\mathbf{x}, t + \Delta t) = \mathcal{F}^{-1}[\hat{\psi}^*(\mathbf{k}, t + \Delta t)]$. After that, $\psi^*(\mathbf{k}, t + \Delta t)$ is normalized to give

$$\psi^{**}(\mathbf{x}, t + \Delta t) = \frac{\psi^*(\mathbf{x}, t + \Delta t)}{\sqrt{\langle \psi^*(\mathbf{x}, t + \Delta t), \psi^*(\mathbf{x}, t + \Delta t) \rangle_{\mathbb{R}}}}. \quad (28)$$

Finally, the wave function $\psi^{**}(\mathbf{x}, t + \Delta t)$ is projected to satisfy the solenoidal condition (5) as $\psi(\mathbf{x}, t + \Delta t) = \psi^{**}(\mathbf{x}, t + \Delta t) \exp(-i\mathbf{q})$, where q is calculated as

$$q = \mathcal{F}^{-1}\left(-\frac{i\mathbf{k} \cdot \mathcal{F}[\mathbf{u}^{**}(\mathbf{x}, t + \Delta t)]}{k^2}\right), \quad (29)$$

with

$$\mathbf{u}^{**}(\mathbf{x}, t + \Delta t) = -\hbar \langle \nabla \psi^{**}(\mathbf{x}, t + \Delta t), i\psi^{**}(\mathbf{x}, t + \Delta t) \rangle_{\mathbb{R}}$$

and

$$\nabla \psi^{**}(\mathbf{x}, t + \Delta t) = \mathcal{F}^{-1}\{i\mathbf{k}\mathcal{F}[\psi^{**}(\mathbf{x}, t + \Delta t)]\}.$$

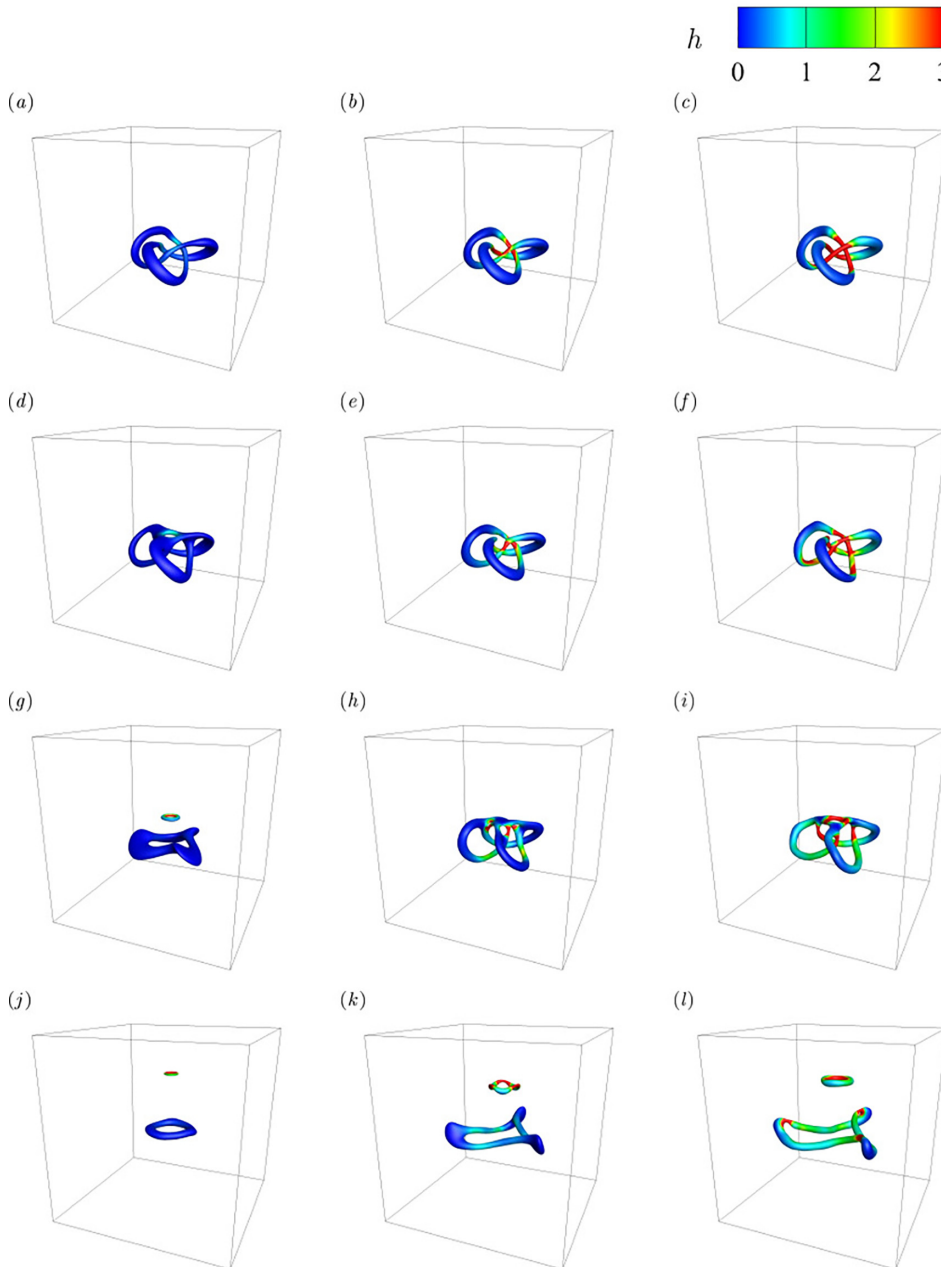


FIG. 7. Isosurfaces of s_1 in the temporal evolution of different trefoil flux tubes with initial conditions T1, T3, and T5 in Table I at $t = 1, 2, 4$, and 8. (a) T1, $t = 1$; (b) T3, $t = 1$; (c) T5, $t = 1$; (d) T1, $t = 2$; (e) T3, $t = 2$; (f) T5, $t = 2$; (g) T1, $t = 4$; (h) T3, $t = 4$; (i) T5, $t = 4$; (j) T1, $t = 8$; (k) T3, $t = 8$; (l) T5, $t = 8$. All the isosurfaces are color-coded by the helicity density. The isocontour values of s_1 are 0.85, 0.6, and 0.25 for T1, T3, and T5, respectively.

V. NUMERICAL RESULTS

A. Grid convergence

To check grid convergence, we set the initial condition as T5 from Table I and test the DNS on three different numbers of grid points: $N^3 = 128^3$, 256^3 , and 512^3 . Figures 5(a), 5(b), and 5(c) plot the kinetic energy spectrum $E(k)$ at $t = 10$ (where k is the wavenumber), the temporal evolution of the volume-averaged kinetic energy E_u , and the writhe, respectively, with three grid resolutions. We see that all curves converge to the curve with grid resolution $N^3 = 512^3$, and the

curves with $N^3 = 256^3$ and 512^3 almost coincide. In the rest of this paper, we take $N^3 = 256^3$ in the numerical simulations.

B. Evolution of flow fields

Figures 6(a) and 6(d) plot the temporal evolution of the normalized kinetic energy $E_u(t)/E_u(t = 0)$. We observe that the normalized kinetic energy decreases monotonically (except for a few minor peaks) in all six cases, which is similar to the energy dissipation in viscous fluids. We remark that the Hamiltonian energy $\hbar^2 \|\nabla \psi\|_{L2}^2 / 2$ of ISF is conserved

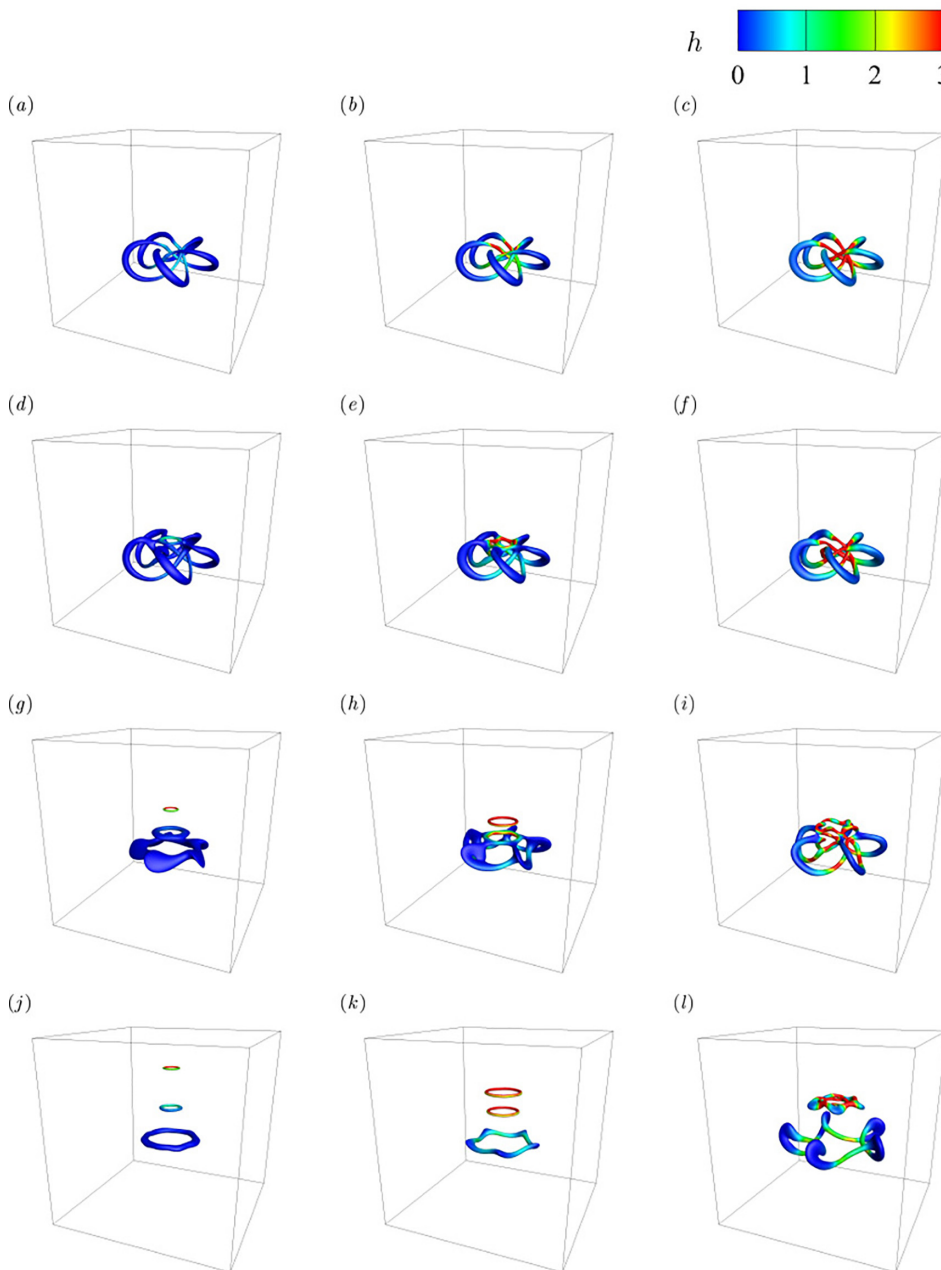


FIG. 8. Isosurfaces of s_1 in the temporal evolution of different trefoil flux tubes with initial conditions C1, C3, and C5 in Table I at $t = 0.5, 1, 3$, and 6 . (a) C1, $t = 0.5$; (b) C3, $t = 0.5$; (c) C5, $t = 0.5$; (d) C1, $t = 1$; (e) C3, $t = 1$; (f) C5, $t = 1$; (g) C1, $t = 3$; (h) C3, $t = 3$; (i) C5, $t = 3$; (j) C1, $t = 6$; (k) C3, $t = 6$; (l) C5, $t = 6$. All the isosurfaces are color-coded by the helicity density. The isocontour values of s_1 are 0.85, 0.6, and 0.25 for C1, C3, and C5, respectively.

during evolution,^{34,37} and so kinetic energy is gradually converted to Landau–Lifshitz energy ($\hbar^2 \|\nabla\psi\|_{L_2}^2 - \|\mathbf{u}\|_{L_2}^2)/2 = \hbar^2 \|\nabla s\|_{L_2}^2/8$.

Figures 6(b) and 6(e) show the temporal evolution of the normalized enstrophy $E_\omega(t)/E_\omega(t=0)$, which is quite different from its evolution in viscous flows.^{45,46,73,74} In all the examples, the normalized enstrophy experiences a rapid decline at first, followed by an upward trend that is accompanied by some fluctuations. These fluctuations are related to topological deformation of the vortex tubes. However, during the critical period of vortex reconnection, the rise in enstrophy is much more moderate than that in viscous flow, indicating that the Landau–Lifshitz term inhibits the energy cascade from large to small scales.^{20,21,23}

In our simulation, the vorticity flux Γ is a conserved quantity (see Appendix C), so the centerline helicity is completely determined by W_r . Figures 6(c) and 6(f) show the temporal evolution of the normalized writhe $W_r/W_r(t=0)$. It is worth noting that although the kinetic energy and enstrophy vary significantly over time, the helicity defined as the integral of the inner product of velocity and vorticity is conserved because the flow can be written in a conservative form convected by the virtual velocity.⁷⁵ Therefore, the change in centerline helicity is converted to twist helicity. As can be seen from Fig. 6(c), for the trefoil knot example, the centerline helicity drops sharply within a short time and varies little before and after this decline. However, in the cinquefoil knot example in Fig. 6(f), the centerline helicity has two sharp declines. These declines in centerline helicity are associated with the untying of the knot, which we will discuss together with the evolution of the knotted field.

In the later stage of evolution, the statistics tend to be stable, which means that the flow is in an equilibrium state of the energy cascade. Thus, although there is no energy input to the dynamical system, it behaves like equilibrium turbulence. From another perspective, the Landau–Lifshitz term also provides a forcing condition to simulate equilibrium turbulence.

Despite the difference in flow statistics, the evolution of the morphological structure of ISF resembles the evolution of knotted vortex tubes in viscous flow. Figures 7 and 8 depict the isosurfaces of s_1 in the temporal evolution of different trefoil and cinquefoil flux tubes with initial conditions given in Table I. All the isosurfaces are color-coded

by helicity density h , which reflects the twisting of local vortex filaments.

Similar to the evolution of trefoil flux tubes in viscous flow, all the trefoil vortex knots first untie into upper and lower vortex rings, with significant vortex reconnection.^{20,21,76–78} Specifically, in the initial stage of vortex reconnection, the vortex tubes in the central part of the trefoil are stretched and then gradually meet, but the topological structure of the knot does not change. Then, the stretched vortex tubes begin to break, with the speed of breaking depending on the twist helicity. Finally, the trefoil begins to untie, forming an upper vortex ring and a lower vortex ring. These two vortex rings gradually change from wavy to flat, which indicates that the center vortex axes become less distorted, which is consistent with the decreasing centerline helicity in Fig. 6(c). We remark that without the participation of viscous forces, intrinsic helicity plays a greater role in flow evolution, which directly changes the reconnection time and the structure scale of the reconnected vortex.

There are some differences in vortex reconnection between trefoil and cinquefoil flux tubes. In cases C1 and C3, the cinquefoil tubes untie twice, eventually forming a state of three vortex rings, which can also be observed in viscous flow.²⁰ Unlike C1 and C3, in C5, a third vortex ring is not formed, and the underlying mechanism may be one in which the intrinsic helicity makes the knotted vortex tube more difficult to untangle.

We also plot the vortex lines inside the cinquefoil knot C3 at different times in Fig. 9. From Fig. 9(a), we can see that the vortex lines inside the vortex tube are nearly parallel at the initial time. The geometric parallelism of the vortex lines indicates that the flow field has a small twist helicity (see Table I). With the evolution of the knotted field, more and more local twisting filamentous structures appear, as shown in Figs. 9(b)–9(d), indicating that the twist is gradually increasing, which is also consistent with the decreasing centerline helicity in Figs. 6(c) and 6(f).

VI. CONCLUSIONS

We have developed a novel method for constructing the initial wave function of knotted vortex tubes to study the evolution of ISF, which is a newly proposed quantized fluid governed by a nonlinear

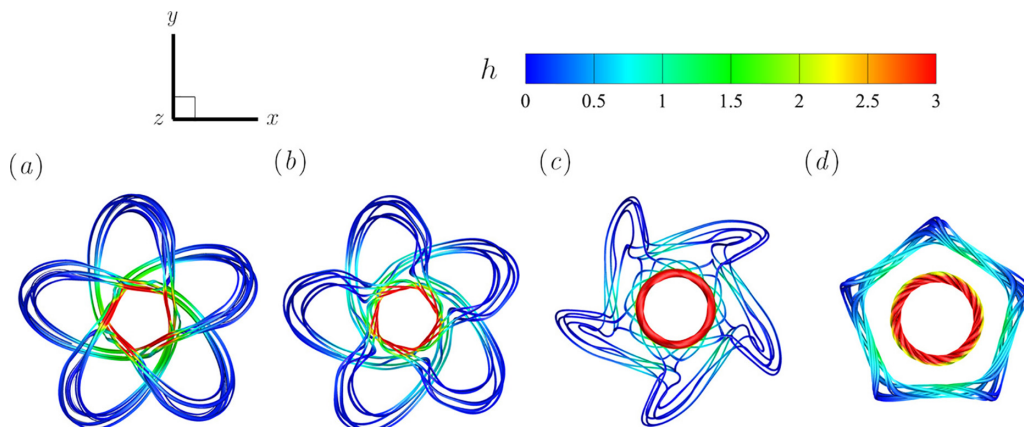


FIG. 9. Internal vortex lines of the cinquefoil knot C3 at different times: (a) $t = 0.5$; (b) $t = 1$; (c) $t = 3$; (d) $t = 6$. The vortex lines are color-coded by helicity density.

Schrödinger equation for a normalized two-component wave function. The constructed fields have finite kinetic energy and enstrophy and can, therefore, be used as the initial states for numerical simulation of fluid evolution. In addition, these constructed fields have tunable helicity, thus providing a natural setting for studying helicity.

We set up six knotted vortex tubes with different centerline and twist helicity as the initial conditions for ISF evolution. For the constructed initial wave functions, we studied the evolution of ISF using DNS based on a pseudospectral method. Similar to the evolution of knotted vortex tubes in viscous flow,^{20,21} all the initial knots become untied after a short time to form one or more separate vortex rings. In contrast to the morphological structure evolution, the difference in statistics is obvious. During the critical period of disconnection and reconnection of the vortex tubes, the rise in enstrophy is much more moderate than that in viscous flows. The Landau–Lifshitz term inhibits the energy cascade from large to small scales,^{20,21,23} thus, the dissipation of kinetic energy in ISF is relatively small. On the other hand, the decay of centerline helicity during reconnection is remarkable, which agrees with the topological changes in vortex lines.

In future work, the construction method for knotted fields will be used to study vortex/magnetic tubes in highly complex configurations. In addition, simulations of ISF with a broader range of initial conditions and flow parameters will be compared to explore the internal dynamics of flow evolution. Furthermore, we know that ISFs are governed by wave field-based incompressible Schrödinger equations, while the viscous flows are governed by the velocity–vorticity field-based Navier–Stokes equations. However, since the constructed initial wave field can be directly converted into the velocity–vorticity field by (6)–(8), we can quantitatively compare the evolution of the knotted vortex tubes in viscous flows and the evolution of ISFs under the same initial conditions. This comparison is significant in helping us to understand the relationship between Landau–Lifshitz and viscous dynamics.

ACKNOWLEDGMENTS

This work was supported by the National Natural Science Foundation of China (Nos. 52071312 and 51939001) and the Liaoning Province Natural Science Foundation Shipping Joint Fund Project (No. 2020-HYLH-29). R. Tao acknowledges the support from the China Scholarship Council visiting research student award.

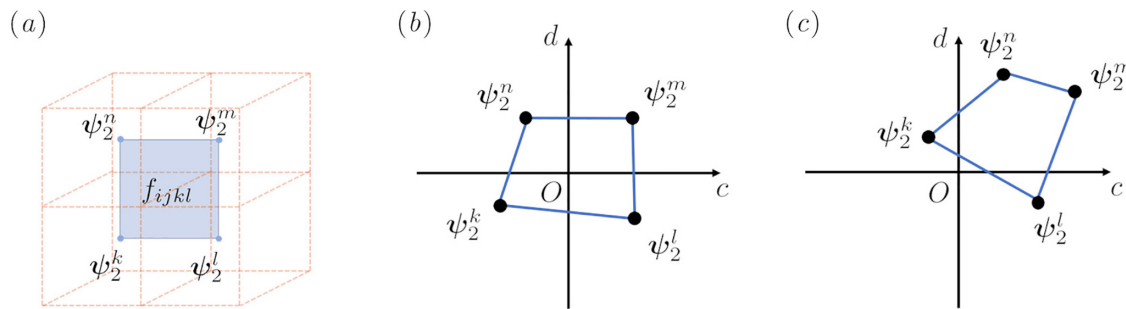


FIG. 10. (a) Quadrilateral formed by the centers of adjacent grids. (b) The origin falls within the quadrilateral. (c) The origin falls outside the quadrilateral.

APPENDIX A: EXTRACTION OF VORTEX AXIS FROM ψ_2

To calculate the centerline helicity of the vortex tube, we need to extract its central vortex axis. In our construction, the central vortex axis of the vortex tube is completely determined by the zero contour line of the wave function component ψ_2 (i.e., the line of intersection of the $c=0$ and $d=0$ isosurfaces). We use the method from Ref. 26 to extract the zero contour of ψ_2 . The basic idea is to use the value of the wave function stored in the center of the grid to get the zero set of the wave function through interpolation. Here, we have made a general assumption that the wave function has zeros only in the plane formed by the centers of the adjacent grids. In Fig. 10(a), the centers of adjacent grids form a quadrilateral. According to the relationship between the zero point and the quadrilateral, there are two possibilities for the relationship: (1) in Fig. 10(b), the zero point falls inside the quadrilateral composed of adjacent grids; (2) in Fig. 10(c), the zero point falls outside the quadrilateral. These two cases can be distinguished by calculating the winding number of the four vertices of the quadrilateral. When the zero point falls inside the quadrilateral, we can calculate the position of the zero point by bilinear interpolation. The method for extracting the zero contour is as follows.

First, we find all the quadrilaterals [see the quadrilaterals f_{ijkl} in Fig. 10(a), on which the discrete values of the wave functions on the four vertices are ψ_2^k , ψ_2^l , ψ_2^m , and ψ_2^n , respectively] that intersect the vortex axis by traversing the centers of adjacent grids in all the regions. Specifically, we can determine whether the vortex axis intersects the quadrilateral by calculating the winding number of the quadrilateral

$$n_{klmn} = \frac{1}{2\pi} \left[\arg\left(\frac{\psi_2^l}{\psi_2^k}\right) + \arg\left(\frac{\psi_2^m}{\psi_2^l}\right) + \arg\left(\frac{\psi_2^n}{\psi_2^m}\right) + \arg\left(\frac{\psi_2^k}{\psi_2^n}\right) \right]. \quad (\text{A1})$$

When the vortex axis intersects a quadrilateral, the origin ($c=0, d=0$) must fall within the quadrilateral, and so the winding number of the plane must be nonzero.

We then calculate the intersection of the vortex axis and the quadrilateral f_{ijkl} . This intersection point can be determined by bilinear interpolation

$$0 = (1 - \lambda_2)[(1 - \lambda_1)\psi_k + \lambda_1\psi_l] + \lambda_2((1 - \lambda_1)\psi_m + \lambda_1\psi_n], \quad (\text{A2})$$

where λ_1 and λ_2 are the interpolation coefficients. We can compute λ_1 and λ_2 by solving the linear equation to get the intersection point. Finally, the order in which intersections connect is determined by the sign of the winding number.

For all the grids intersecting the vortex axis, we can find at least a pair of points that are the intersection points of the vortex axis and a grid. The sign of n_{klmn} in (A1) exactly represents the entry ($n_{klmn} = -1$) and exit ($n_{klmn} = +1$) of the vortex axis. Connecting the intersection points of opposite signs in each grid gives the desired vortex axis. After extracting the discrete points of the central vortex axis, we use the least squares method to calculate the physical quantities needed. For the constructed cases, the values are listed in Table I.

APPENDIX B: DERIVATION OF ISF EQUATION

This appendix shows that Eq. (23) is equivalent to Eq. (26). Inspired by the method given in Ref. 34, we propose the following proof. Assuming that the wave function satisfies Eq. (26), we start from the quaternionic form of the wave function and use the relationship between the rotation vector s , the velocity field u , and the wave function ψ to eventually obtain Eq. (23). The quaternionic form of the wave function ψ is

$$\psi = a + bi + cj + dk, \quad (\text{B1})$$

where i , j , and k are the basis elements of the imaginary part of the quaternion. Based on the relationship between the rotation vector s and the wave function ψ shown in Fig. 1, the spin vector and its gradient can be expressed as

$$\begin{cases} s = \bar{\psi}i\psi, \\ \nabla s = (\nabla\bar{\psi})i\psi + \bar{\psi}i(\nabla\psi). \end{cases} \quad (\text{B2})$$

From Eq. (7), we obtain another form of the wave function representation of the velocity

$$u = \frac{\hbar}{2}(\nabla\bar{\psi}i\psi - \bar{\psi}i\nabla\psi). \quad (\text{B3})$$

From Eqs. (B2) and (B3), we obtain the gradient of ψ

$$\nabla\psi = i\psi\left(\frac{u}{\hbar} - \frac{1}{2}\nabla s\right). \quad (\text{B4})$$

We then calculate the divergence of Eq. (B4). We combine Eqs. (B2), (B3), and the zero-divergence condition on the velocity field to obtain the Laplacian of ψ

$$\begin{aligned} \nabla^2\psi &= i(\nabla\psi)\cdot\frac{u}{\hbar} - \frac{1}{2}i(\nabla\psi)\cdot(\nabla s) - \frac{1}{2}i\psi\Delta s \\ &= i(\nabla\psi)\cdot\frac{u}{\hbar} + i(\nabla\psi)\cdot\left(\frac{u}{\hbar} - \nabla\bar{\psi}i\psi\right) - \frac{1}{2}\psi\bar{\psi}i\psi\Delta s \\ &= \frac{2i}{\hbar}u\cdot\nabla\psi - i(\nabla\psi)\cdot(\nabla\bar{\psi}i\psi) - \frac{1}{2}\psi s\Delta s \\ &= \frac{2i}{\hbar}u\cdot\nabla\psi + \psi\left(|\nabla\psi|^2 - \frac{1}{2}s\Delta s\right) \\ &= \frac{2i}{\hbar}u\cdot\nabla\psi + \psi\left[\left(|\nabla\psi|^2 + \frac{1}{2}\langle s, \Delta s \rangle\right) - \frac{1}{2}(s \times \Delta s)\right]. \end{aligned} \quad (\text{B5})$$

In Eq. (B5), $\langle \psi, \phi \rangle = \text{Re}(\bar{\psi}\phi)$ is the quaternionic inner product. The purpose of calculating $\nabla^2\psi$ is to obtain a relationship between $\frac{1}{2}i\hbar\nabla^2\psi$ and $u \cdot \nabla\psi$.

$$i\frac{\hbar}{2}\nabla^2\psi = -u \cdot \nabla\psi + i\frac{\hbar}{2}\psi\left[\left(|\nabla\psi|^2 + \frac{1}{2}\langle s, \Delta s \rangle_C\right) - \frac{1}{2}(s \times \Delta s)\right]. \quad (\text{B6})$$

We then substitute Eq. (B6) into Eq. (26) and get

$$\frac{\partial\psi}{\partial t} + u \cdot \nabla\psi = -i\psi\left[\frac{\hbar}{4}(s \times \Delta s) + \tilde{p}\right], \quad (\text{B7})$$

where \tilde{p} is the modified pressure,

$$\tilde{p} = \frac{p}{\hbar} - \frac{\hbar}{2}|\nabla\psi|^2 - \frac{\hbar}{4}\langle s, \Delta s \rangle. \quad (\text{B8})$$

Finally, we apply $-\bar{\psi}i\nabla$ to the left- and right-hand sides of Eq. (B7) and then take the real part to get Eq. (23). The calculation process for the left-hand side of the equation is

$$\begin{aligned} &\text{Re}\left[-\bar{\psi}i\nabla\left(\frac{\partial\psi}{\partial t} + u \cdot \nabla\psi\right)\right] \\ &= \frac{1}{\hbar}\frac{\partial u}{\partial t} + \text{Re}\left[\frac{\partial\bar{\psi}}{\partial t}i\nabla\psi - \bar{\psi}i\nabla(u \cdot \nabla\psi)\right] \\ &= \frac{1}{\hbar}\left(\frac{\partial u}{\partial t} + \nabla\frac{|u|^2}{2}\right) + \text{Re}\left[\frac{\partial\bar{\psi}}{\partial t}i\nabla\psi - \bar{\psi}iu \cdot (\nabla\nabla\psi)\right] \\ &= \frac{1}{\hbar}\left(\frac{\partial u}{\partial t} + \nabla\frac{|u|^2}{2}\right) \\ &\quad + \text{Re}\left[\frac{\partial\bar{\psi}}{\partial t}i\nabla\psi - u \cdot \nabla(\bar{\psi}i\nabla\psi) + u \cdot (\nabla\bar{\psi})i(\nabla\psi)\right] \\ &= \frac{1}{\hbar}\left(\frac{\partial u}{\partial t} + u \cdot \nabla u + \frac{\nabla|u|^2}{2}\right) \\ &\quad + \text{Re}\left[\left(\frac{\partial\bar{\psi}}{\partial t} + u \cdot \nabla\bar{\psi}\right)i\nabla\psi\right] \\ &= \frac{1}{\hbar}\left(\frac{\partial u}{\partial t} + u \cdot \nabla u + \frac{\nabla|u|^2}{2}\right) \\ &\quad - \text{Re}\left[\left(\tilde{p} - \frac{\hbar}{4}s \times \Delta s\right)\bar{\psi}\nabla\psi\right] \\ &= \frac{1}{\hbar}\left(\frac{\partial u}{\partial t} + u \cdot \nabla u + \frac{\nabla|u|^2}{2}\right) - \frac{\hbar}{4}\text{Re}[(\Delta s)s\bar{\psi}\nabla\psi] \\ &= \frac{1}{\hbar}\left(\frac{\partial u}{\partial t} + u \cdot \nabla u + \frac{\nabla|u|^2}{2}\right) + \frac{\hbar}{8}\langle\nabla s, \Delta s\rangle. \end{aligned} \quad (\text{B9})$$

The calculation process for the right-hand side of the equation is

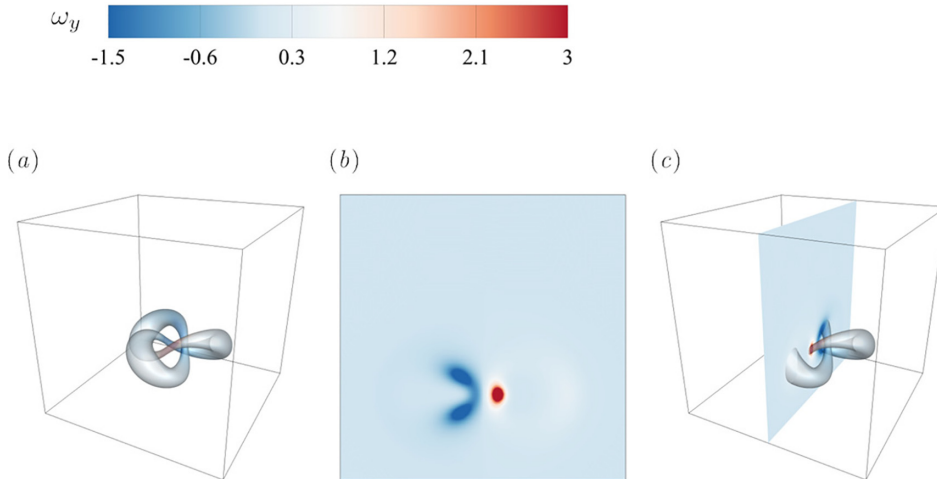


FIG. 11. Schematic of the calculation of vorticity fluxes. Isosurfaces are color-coded by ω_y . (a) Isosurfaces of s_1 . (b) Plane cut of the contour of ω_y . (c) Integration of (a) and (b).

$$\begin{aligned}
 & \operatorname{Re} \left\{ -\bar{\psi} i \nabla \left[-i \bar{\psi} \left(\frac{\hbar}{4} \mathbf{s} \times \Delta \mathbf{s} + \tilde{p} \right) \right] \right\} \\
 &= -\operatorname{Re} \left\{ \bar{\psi} \nabla \left[\bar{\psi} \left(\frac{\hbar}{4} \mathbf{s} \times \Delta \mathbf{s} + \tilde{p} \right) \right] \right\} \\
 &= -\operatorname{Re} \left[\bar{\psi} (\nabla \bar{\psi}) \left(\frac{\hbar}{4} \mathbf{s} \times \Delta \mathbf{s} + \tilde{p} \right) \right] - \nabla \tilde{p} \\
 &= -\frac{\hbar}{4} \operatorname{Re} [\bar{\psi} (\nabla \bar{\psi}) \mathbf{s} \Delta \mathbf{s}] - \nabla \tilde{p} \\
 &= \frac{\hbar}{4} \operatorname{Re} [(\nabla \bar{\psi}) \bar{\psi} \mathbf{s} \Delta \mathbf{s}] - \nabla \tilde{p} \\
 &= \frac{\hbar}{8} \operatorname{Re} [(\nabla \mathbf{s}) \Delta \mathbf{s}] - \nabla \tilde{p} \\
 &= -\frac{\hbar}{8} \langle \nabla \mathbf{s}, \Delta \mathbf{s} \rangle - \nabla \tilde{p}. \tag{B10}
 \end{aligned}$$

We combine Eq. (B9) with Eq. (B10) to get

$$\frac{\partial \mathbf{u}}{\partial t} + \mathbf{u} \cdot \nabla \mathbf{u} = -\hbar \nabla \left(\tilde{p} + \frac{\nabla |\mathbf{u}|^2}{2} \right) - \frac{\hbar^2}{4} \langle \nabla \mathbf{s}, \Delta \mathbf{s} \rangle, \tag{B11}$$

which is Eq. (23).

APPENDIX C: COMPUTATION OF VORTICITY FLUXES

For the ISF governed by Eq. (23), the vorticity fluxes are conserved during the evolutionary process. We select the plane section at $y = \pi$, and the vorticity fluxes of the closed knotted vortex tube passing through this section can be divided into four parts, as shown in Fig. 11. We calculate the sum of the absolute vorticity fluxes on the section and then divide this by four. The result is the vorticity fluxes of the knotted tube. The conservation of vorticity fluxes in the evolutionary process is proved as follows.⁷⁵

Theorem 1. Let $S(t)$ be a virtual material surface advected by a virtual velocity

$$\mathbf{v} = \mathbf{u} + \frac{\hbar^2}{4} \frac{\langle \nabla \mathbf{s}, \Delta \mathbf{s} \rangle \times \boldsymbol{\omega}}{|\boldsymbol{\omega}|^2}. \tag{C1}$$

The circulation is then a virtual Lagrangian scalar, since

$$\frac{D_v \Gamma}{D_v t} = 0, \tag{C2}$$

where $D_v/D_v t = \partial/\partial t + \mathbf{v} \cdot \nabla$ is the virtual material derivative.

Proof. By acting on both sides of Eq. (B11) with the operator $\nabla \times$, we obtain

$$\frac{\partial \boldsymbol{\omega}}{\partial t} = \nabla \times (\mathbf{v} \times \boldsymbol{\omega}). \tag{C3}$$

Therefore, the change in vorticity flux with time through $S(t)$ can be calculated as

$$\begin{aligned}
 \frac{D_v \Gamma}{D_v t} &= \frac{d}{dt} \int_{S(t)} \boldsymbol{\omega} \cdot d\mathbf{S} \\
 &= \int_{S(t)} \left[\frac{D_v \boldsymbol{\omega}}{D_v t} + \boldsymbol{\omega} \cdot (\nabla \cdot \mathbf{v} - \nabla \cdot \mathbf{v}) \right] \cdot d\mathbf{S} \\
 &= \int_{S(t)} \left[\frac{\partial \boldsymbol{\omega}}{\partial t} - \nabla \times (\mathbf{v} \times \boldsymbol{\omega}) \right] \cdot d\mathbf{S} \\
 &= 0. \tag{C4}
 \end{aligned}$$

DATA AVAILABILITY

The data that support the findings of this study are available from the corresponding author upon reasonable request.

REFERENCES

- A. Enciso, D. Peralta-Salas, and F. T. de Lizaur, “Helicity is the only integral invariant of volume-preserving transformations,” *Proc. Natl. Acad. Sci. U.S.A.* **113**, 2035–2040 (2016).
- M. W. Scheeler, W. M. van Rees, H. Kedia, D. Kleckner, and W. T. M. Irvine, “Complete measurement of helicity and its dynamics in vortex tube,” *Science* **357**, 487–491 (2017).
- H. K. Moffatt, “Helicity-invariant even in a viscous fluid,” *Science* **357**(6350), 448 (2017).

- ⁴R. M. Kerr, "Trefoil knot timescales for reconnection and helicity," *Fluid Dyn. Res.* **50**, 011422 (2018).
- ⁵J. J. Moreau, "Constantes d'un îlot tourbillonnaire en fluide parfait barotrope," *C.R. Acad. Sci. Paris* **252**, 2810–2812 (1961).
- ⁶D. Kleckner and W. T. M. Irvine, "Creation and dynamics of knotted vortices," *Nat. Phys.* **9**, 253–258 (2013).
- ⁷F. Hussain and M. V. Melander, "New aspects of vortex dynamics: Helical waves, core dynamics, viscous helicity generation, and interaction with turbulence," in *Topological Aspects of the Dynamics of Fluids and Plasmas* (Springer, 1992), pp. 377–399.
- ⁸P. Koumoutsakos, A. Leonard, and F. Pepin, "Boundary conditions for viscous vortex methods," *J. Comput. Phys.* **113**, 52–61 (1994).
- ⁹R. M. Kerr, "Enstrophy and circulation scaling for Navier-Stokes reconnection," *J. Fluid Mech.* **839**, R2 (2018).
- ¹⁰R. L. Ricca and H. K. Moffatt, "The helicity of a knotted vortex filament," in *Topological Aspects of the Dynamics of Fluids and Plasmas* (Springer, 1992), pp. 225–236.
- ¹¹H. Kedia, I. Bialynicki-Birula, D. Peralta-Salas, and W. T. M. Irvine, "Tying knots in light fields," *Phys. Rev. Lett.* **111**, 150404 (2013).
- ¹²J. Hao and Y. Yang, "Magnetic knot cascade via the stepwise reconnection of helical flux tubes," *J. Fluid Mech.* **912**, A48 (2021).
- ¹³A. Martinez, M. Ravnik, B. Lucero, R. Visvanathan, S. Zumer, and I. I. Smalyukh, "Mutually tangled colloidal knots and induced defect loops in nematic fields," *Nat. Mater.* **13**, 258–263 (2014).
- ¹⁴M. R. Dennis, R. P. King, B. Jack, K. O'Holleran, and M. J. Padgett, "Isolated optical vortex knots," *Nat. Phys.* **6**, 118–121 (2010).
- ¹⁵D. Han, S. Pal, Y. Liu, and H. Yan, "Folding and cutting DNA into reconfigurable topological nanostructures," *Nat. Nanotechnol.* **5**, 712–717 (2010).
- ¹⁶K. S. Chichak, S. J. Cantrill, A. R. Pease, S.-H. Chiu, G. W. Cave, J. L. Atwood, and J. F. Stoddart, "Molecular Borromean rings," *Science* **304**, 1308–1312 (2004).
- ¹⁷D. W. Sumners, "Lifting the curtain: Using topology to probe the hidden action of enzymes," *Not. Am. Math. Soc.* **42**, 528–537 (1995).
- ¹⁸T. Vachaspati and G. B. Field, "Electroweak string configurations with Baryon number," *Phys. Rev. Lett.* **73**, 373 (1994).
- ¹⁹J. D. Bekenstein, "Conservation law for linked cosmic string loops," *Phys. Lett. B* **282**, 44–49 (1992).
- ²⁰S. Xiong and Y. Yang, "Construction of knotted vortex tubes with the writhe-dependent helicity," *Phys. Fluids* **31**, 047101 (2019).
- ²¹S. Xiong and Y. Yang, "Effects of twist on the evolution of knotted magnetic flux tubes," *J. Fluid Mech.* **895**, A28 (2020).
- ²²H. K. Moffatt and R. L. Ricca, "Helicity and the Călugăreanu invariant," *Proc. R. Soc. London, Ser. A* **439**, 411–429 (1992).
- ²³S. Xiong and Y. Yang, "Evolution and helicity analysis of linked vortex tubes in viscous flows," *Sci. Sin. Phys. Mech. Astron.* **50**, 040005 (2020).
- ²⁴M. Bergou, M. Wardetzky, S. Robinson, B. Audoly, and E. Grinspun, "Discrete elastic rods," *ACM Trans. Graphics* **27**, 3 (2008).
- ²⁵M. A. Berger and G. B. Field, "The topological properties of magnetic helicity," *J. Fluid Mech.* **147**, 133–148 (1984).
- ²⁶S. Weißmann, U. Pinkall, and P. Schröder, "Smoke rings from smoke," *ACM Trans. Graphics* **33**, 140 (2014).
- ²⁷E. Madelung, "Eine anschauliche Deutung der Gleichung von Schrödinger," *Naturwissenschaften* **14**, 1004 (1926).
- ²⁸E. Madelung, "Quantentheorie in hydrodynamischer form," *Z. Phys.* **40**, 322–326 (1927).
- ²⁹H. Hasimoto, "A soliton on a vortex filament," *J. Fluid Mech.* **51**, 477–485 (1972).
- ³⁰E. J. Hopfinger, F. K. Browand, and Y. Gagne, "Turbulence and waves in a rotating tank," *J. Fluid Mech.* **125**, 505–534 (1982).
- ³¹H. Aref, "Stirring by chaotic advection," *J. Fluid Mech.* **143**, 1–21 (1984).
- ³²M. Schönberg, "On the hydrodynamical model of the quantum mechanics," *Nuovo Cimento* **12**, 103–133 (1954).
- ³³A. L. Sorokin, "Madelung transformation for vortex flows of a perfect liquid," *Dokl. Phys.* **46**, 576–578 (2001).
- ³⁴A. Chern, F. Knöppel, U. Pinkall, P. Schröder, and S. Weißmann, "Schrödinger's smoke," *ACM Trans. Graphics* **35**, 77 (2016).
- ³⁵G. A. Kuz'min, "Ideal incompressible hydrodynamics in terms of the vortex momentum density," *Phys. Lett. A* **96**, 88–90 (1983).
- ³⁶A. J. Niemi and P. Sutcliffe, "Leapfrogging vortex rings in the Landau–Lifshitz equation," *Nonlinearity* **27**, 2095–2109 (2014).
- ³⁷A. Chern, F. Knöppel, U. Pinkall, and P. Schröder, "Inside fluids: Clebsch maps for visualization and processing," *ACM Trans. Graphics* **36**, 142 (2017).
- ³⁸H. Kedia, D. Foster, M. R. Dennis, and W. T. M. Irvine, "Weaving knotted vector fields with tunable helicity," *Phys. Rev. Lett.* **117**, 274501 (2016).
- ³⁹G. Hao, Z. Simone, R. Ricca, and X. Liu, "Topological fluid mechanics and its new developments," *Sci. Sin. Phys. Mech. Astron.* **50**, 054701 (2020).
- ⁴⁰Z. Q. Xin and C. J. Wu, "Shape optimization of the caudal fin of the three-dimensional self-propelled swimming fish," *Sci. Sin. Phys. Mech. Astron.* **56**, 328–339 (2013).
- ⁴¹J. Z. Zhu, "Vorticity and helicity decompositions and dynamics with real Schur form of the velocity gradient," *Phys. Fluids* **30**, 031703 (2018).
- ⁴²S. Zuccher and R. L. Ricca, "Relaxation of twist helicity in the cascade process of linked quantum vortices," *Phys. Rev. E* **95**, 053109 (2017).
- ⁴³C. Oberti and R. L. Ricca, "Influence of winding number on vortex knots dynamics," *Sci. Rep.* **9**, 17284 (2019).
- ⁴⁴R. S. Rogallo, "Numerical experiments in homogeneous turbulence," Technical Report No. TM81315 (NASA, 1981).
- ⁴⁵M. W. Scheeler, D. Kleckner, D. Proment, G. L. Kindlmann, and W. T. M. Irvine, "Helicity conservation by flow across scales in reconnecting vortex links and knots," *Proc. Natl. Acad. Sci. U.S.A.* **111**, 15350–15355 (2014).
- ⁴⁶S. Kida and M. Takaoka, "Vortex reconnection," *Annu. Rev. Fluid Mech.* **26**, 169–189 (1994).
- ⁴⁷J. Yao and F. Hussain, "A physical model of turbulence cascade via vortex reconnection sequence and avalanche," *J. Fluid Mech.* **883**, A51 (2020).
- ⁴⁸P. Chatelain, D. Kivotides, and A. Leonard, "Reconnection of colliding vortex rings," *Phys. Rev. Lett.* **90**, 054501 (2003).
- ⁴⁹V. L. Nguyen and V. D. Duong, "Vortex ring-tube reconnection in a viscous fluid," *Phys. Fluids* **33**, 015122 (2021).
- ⁵⁰M. Cheng, J. Lou, and T. Lim, "Collision and reconnection of viscous elliptic vortex rings," *Phys. Fluids* **31**, 067107 (2019).
- ⁵¹S. Leibovich, "The structure of vortex breakdown," *Annu. Rev. Fluid Mech.* **10**, 221–246 (1978).
- ⁵²S. Xiong and Y. Yang, "Identifying the tangle of vortex tubes in homogeneous isotropic turbulence," *J. Fluid Mech.* **874**, 952–978 (2019).
- ⁵³A. Clebsch, "Über die Integration der hydrodynamischen Gleichungen," *J. Reine Angew. Math.* **56**, 1–10 (1859).
- ⁵⁴H. Lamb, *Hydrodynamics*, 6th ed. (Cambridge University Press, 1932).
- ⁵⁵Y. Yang and D. I. Pullin, "On Lagrangian and vortex-surface fields for flows with Taylor–Green and Kida–Pelz initial conditions," *J. Fluid Mech.* **661**, 446–481 (2010).
- ⁵⁶W. Tong, Y. Yang, and S. Wang, "Estimating thrust from shedding vortex surfaces in the wake of a flapping plate," *J. Fluid Mech.* **920**, A10 (2021).
- ⁵⁷W. Tong, Y. Yang, and S. Wang, "Characterizing three-dimensional features of vortex surfaces in the flow past a finite plate," *Phys. Fluids* **32**, 011903 (2020).
- ⁵⁸P. R. Kotiuga, "Clebsch potentials and the visualization of three-dimensional solenoidal vector fields," *IEEE Trans. Magn.* **27**, 3986–3989 (1991).
- ⁵⁹J. Jeong and F. Hussain, "On the identification of a vortex," *J. Fluid Mech.* **285**, 69–94 (1995).
- ⁶⁰A. Brandenburg, "Magnetic field evolution in simulations with Euler potentials," *Mon. Not. R. Astron. Soc.* **401**, 347–354 (2010).
- ⁶¹C. Cartes, M. D. Bustamante, and M. E. Brachet, "Generalized Eulerian–Lagrangian description of Navier–Stokes dynamics," *Phys. Fluids* **19**, 077101 (2007).
- ⁶²E. A. Kuznetsov and A. V. Mikhailov, "On the topological meaning of canonical Clebsch variables," *Phys. Lett. A* **77**, 37–38 (1980).
- ⁶³H. Hopf, "Über die Abbildungen der Dreidimensionalen Sphäre auf die Kugelfläche," *Math. Ann.* **104**, 637–665 (1931).
- ⁶⁴Y. Yang and D. I. Pullin, "Evolution of vortex-surface fields in viscous Taylor–Green and Kida–Pelz flows," *J. Fluid Mech.* **685**, 146–164 (2011).
- ⁶⁵Y. Zhao, Y. Yang, and S. Chen, "Vortex reconnection in the late transition in channel flow," *J. Fluid Mech.* **802**, R4 (2016).
- ⁶⁶Y. Zhao, S. Xiong, Y. Yang, and S. Chen, "Sinuous distortion of vortex surfaces in the lateral growth of turbulent spots," *Phys. Rev. Fluids* **3**, 074701 (2018).
- ⁶⁷S. Xiong and Y. Yang, "The boundary-constraint method for constructing vortex-surface fields," *J. Comput. Phys.* **339**, 31–45 (2017).

- ⁶⁸A. Zandian, W. A. Sirignano, and F. Hussain, "Understanding liquid-jet atomization cascades via vortex dynamics," *J. Fluid Mech.* **843**, 293–354 (2018).
- ⁶⁹M. M. Hejlesen, P. Koumoutsakos, A. Leonard, and J. H. Walther, "An improved interface penalisation for vortex methods," in Proceedings of the 3rd International Conference on Particle-Based Methods (2013).
- ⁷⁰S. Zou, W.-K. Bai, T. Yang, and W.-M. Liu, "Formation of vortex rings and hopfions in trapped Bose-Einstein condensates," *Phys. Fluids* **33**, 027105 (2021).
- ⁷¹A. Leonard, "On the motion of thin vortex tubes," *Theor. Comput. Fluid Dyn.* **24**, 369–375 (2010).
- ⁷²W. M. Van Rees, A. Leonard, D. I. Pullin, and P. Koumoutsakos, "A comparison of vortex and pseudo-spectral methods for the simulation of periodic vortical flows at high Reynolds numbers," *J. Comput. Phys.* **230**, 2794–2805 (2011).
- ⁷³F. Hussain and K. Duraisamy, "Mechanics of viscous vortex reconnection," *Phys. Fluids* **23**, 021701 (2011).
- ⁷⁴X. Liu and R. L. Ricca, "Knots cascade detected by a monotonically decreasing sequence of values," *Sci. Rep.* **6**, 24118 (2016).
- ⁷⁵J. Hao, S. Xiong, and Y. Yang, "Tracking vortex surfaces frozen in the virtual velocity in non-ideal flows," *J. Fluid Mech.* **863**, 513–544 (2019).
- ⁷⁶J. Yao and F. Hussain, "On singularity formation via viscous vortex reconnection," *J. Fluid Mech.* **888**, R2 (2020).
- ⁷⁷J. Yao and F. Hussain, "Separation scaling for viscous vortex reconnection," *J. Fluid Mech.* **900**, R4 (2020).
- ⁷⁸R. M. Kerr, "Swirling, turbulent vortex rings formed from a chain reaction of reconnection events," *Phys. Fluids* **25**, 065101 (2013).